Photoemission and degradation of semiconductor photocathode

Peng-Wei Huang,[1] Houjun Qian,[2] Yingchao Du,[1] Wenhui Huang,[1]
Zhen Zhang,[1] and Chuanxiang Tang[1,*]

[1]*Department of Engineering Physics, Tsinghua University, Beijing 100084, China*
[2]*Deutsches Elektronen-Synchrotron DESY, Platanenallee 6, 15738 Zeuthen, Germany*

(Received 15 November 2018; published 23 December 2019)

In state of the art photoemission electron sources, the transverse emittance of the electron beam is approaching its intrinsic value from the cathode. To reduce the intrinsic emittance, it is straightforward to tune the photon energy of the drive laser toward the photocathode emission threshold. This paper aims at constructing an improved model which takes into account an intermediate energy level to better explain the near threshold photoemission for semiconductors. A dynamic model is also proposed to evaluate the cathode degradation process due to surface oxidation. The models agree well with published results for different materials under various conditions, including electric field, temperature and vacuum condition. The dynamic model predicts that near threshold emission of an oxidized Cs_3Sb cathode outperforms UV photoemission of typical metal cathodes in terms of both quantum efficiency and intrinsic emittance. With the oxidization layer, the robustness of semiconductor cathodes to gun vacuum condition may be comparable to a metal cathode. This, however, needs further testing.

DOI: 10.1103/PhysRevAccelBeams.22.123403

I. INTRODUCTION

High brightness electron beams have enabled most powerful scientific instruments, including for example x-ray free electron lasers (XFEL) and ultrafast electron diffraction (UED), for cutting edge research in ultrafast science [1–6]. Reducing the emittance of electron beams is highly desired to improve the performance of these instruments. In state of the art photoemission electron sources, the cathode sets ultimate limits on achievable beam quality. Therefore lowering the intrinsic emittance is of vital importance in both the FEL and UED communities [7–9].

To achieve lower intrinsic emittance from photocathodes, one of the promising approaches is to vary the wavelength of driven laser to approach the photoemission threshold [10–15]. For metal cathodes, the intrinsic emittance can be barely below 0.5 mm mrad per mm laser spot size (rms) [10,14] by tuning the laser wavelength, constrained by keeping a reasonable quantum efficiency (QE). For semiconductors, the intrinsic emittance can be lower (0.2–0.3 mm mrad/mm rms) when the incident photon energy is near or below the threshold [11–13], while QE still supports low average photoelectron current operation. Some previous work has studied the photoemission mechanisms of semiconductors [16–19], but deviations still exist between theories and experiments. Moreover, the semiconductor is less robust against poisoning by the residual gases and has a relatively short lifetime in practice, and a dynamical model to investigate the cathode performance during the degradation process is still missing.

This paper will propose a dynamic model for the cathode degradation process due to residual gases. The cathode degradation by ion back bombardment is not considered in this model. Previous works have reported the decay of cathodes' QE with the presence of "poisonous" gases, like O_2, H_2O, CO_2. Some studies have been dedicated on the chemical analysis of surface reactivity of common residual gas molecules [20]. The conclusion was that the oxygen has the most detrimental effect on QE. However, the dynamics of the degradation process was not discussed. Exponential fitting is a standard method used to evaluate the degradation of the QE [21,22], while clear deviation of the entire degradation process from the exponential trend was observed [23,24]. Pavlenko and coworkers suggested to include an intermediate and reversible physisorption step to account for the discrepancy. Their model provided new insights into the physical picture of the degradation of QE for various materials, but the behavior of the intrinsic emittance was not discussed [23]. It has been confirmed experimentally that as the QE decays continuously with the accumulated oxygen dose, the intrinsic emittance would experience a reduction for GaAsP [25]. Hence it is reasonable to expect a possible correlation between intrinsic emittance and QE degradation.

*tang.xuh@tsinghua.edu.cn

In this paper, a static model is first introduced to describe the semiconductor photoemission process in steady state with the consideration of the acceptor level. Then a dynamic model is proposed to describe the cathode degradation process due to residual gases and it analyzes the evolution of quantum efficiency and intrinsic emittance. The static model is capable of reproducing the QE and mean transverse energy of Cs_3Sb near threshold emission under low electric field and different temperature. The dynamic model is applied to the evolution of cathode performance for Cs_3Sb and GaAsP due to oxygen absorption. The simulations show the oxidized Cs_3Sb at threshold photoemission might be able to replace metal cathodes with UV photoemission, with the advantages of higher QE and lower intrinsic emittance. Oxidized semiconductor cathode might have comparable tolerance to gun vacuum condition as metal cathodes, which can be benchmarked with future experiments.

II. STATIC MODEL

The photoemission model presented in this paper is displayed in Fig. 1. It is based on the three step model [16,17,26]. The major differences lie in the consideration of the contribution from the acceptor level located at the band gap and the energy loss caused by scattering with the crystal lattice in the analytical model. The band bending region near the surface can alter the energy band and affect the electrons emission. If the material is p-typed bulk with n-typed surface, a shallow p-n junction will be formed near the surface and the electric field helps to extract electrons, reducing the effective barrier as shown in Fig. 1. Many commonly used photocathodes are p-typed semiconductors and have similar structures, like Cs_3Sb, K_2CsSb, GaAs. With the acceptor density N_A and the width of band bending region d_b, the bending energy E_b can be estimated through [27]

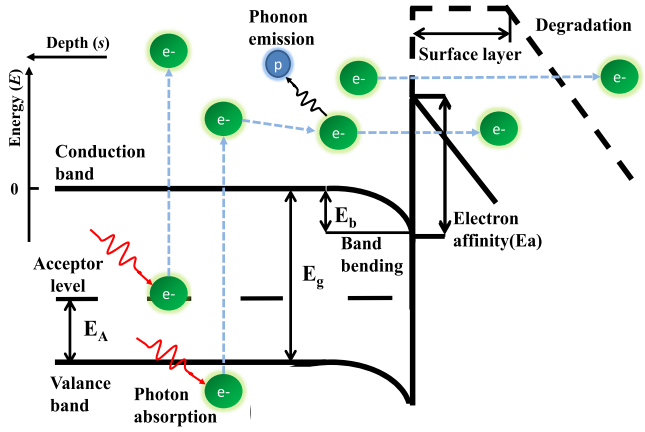

FIG. 1. Photoemission of semiconductors. The dash part at the surface side is the proposed model for degradation.

$$E_b = \frac{eN_A d_b^2}{2\varepsilon_s \varepsilon_0}, \tag{1}$$

where ε_s is the material's relative permittivity, ε_0 is the vacuum permittivity and e is the elementary charge.

There are two origins of electrons from the bulk. One is the valance band, which is included in most of the models. The other is the acceptor level. The lattice imperfections, like foreign atoms or vacancies, can lead to the formation of the acceptor level in the band gap. The contribution from the acceptor level is usually not considered. In the following we discuss the effects of the acceptor level in the photoemission process. The Fermi level of the materials is important to determine the distribution of electrons and it is usually located at the gap between the conduction band and valance band for semiconductors. Since there is lack of record about the Fermi level for many semiconductors, for simplicity, we follow the common rule discovered from most of the III-V type semiconductors, and assume that the Fermi energy of the surface state is fixed at one third of the band gap [28,29]. As a stable and complete system, the Fermi level of the bulk should be the same as that at the surface. This can be achieved through band bending. Therefore the difference between the bulk and the surface Fermi energy is E_b. Consequently, the bulk Fermi level E_F, with respect to the top of the bulk valance band, is

$$E_F = E_g/3 - E_b. \tag{2}$$

With the assumed Fermi energy above, the possibility of electrons occupied at the acceptor level can be evaluated following the Fermi distribution [28],

$$f_A(E_A) = \frac{1}{1 + 2\exp\left[(E_A - E_F)/k_B T\right]} \tag{3}$$

where E_A is the energy of the acceptor level above the top of the valance band, and E_F is the bulk Fermi energy. k_B and T are Boltzman parameter and temperature respectively. Therefore, the contribution from the acceptor level will be $N_A \cdot f_A(E_A)$.

In the valance band, the energy state density of the electrons is proportional to the square root of energy relative to the top of the band in the simple free electron Fermi gas model [30]. In the conduction band, the square root law is still valid, except that the energy of the state is defined relative to the bottom of the band. Therefore the expression for the density of electrons per unit of energy [30] is

$$D_e(E) = \begin{cases} \frac{1}{2\pi^2}\left(\frac{2m_0}{\hbar^2}\right)^{\frac{3}{2}}\sqrt{-E_g - E}, & E < -E_g \\ \frac{1}{2\pi^2}\left(\frac{2m_0}{\hbar^2}\right)^{\frac{3}{2}}\sqrt{E}, & E > 0 \end{cases} \tag{4}$$

where $\hbar$ is the Plank parameter and m_0 is the rest electron mass. E refers to the energy of electrons. Here the energy at the bottom of conduction band is set to zero, shown in Fig. 1.

The possibility of electrons excited from energy $E-\hbar\omega$ to E is the product of the density of filled states at $E-\hbar\omega$, $D_e(E-\hbar\omega)f_e(E-\hbar\omega+E_g)$, and the density of empty states at E, $D_e(E)(1-f_e(E+E_g))$ [31]. Here $f_e(E)$ is the Fermi-Dirac function at energy E for valance and conduction band and has the expression as

$$f_e(E)=\frac{1}{1+\exp\left[(E-E_F)/k_BT\right]}. \tag{5}$$

At 300 K, the k_BT is roughly 26 meV, which is usually much smaller than the energy difference between the Fermi energy and the valance band or the conduction band among our interested photocathode materials. Therefore $f_e(E-\hbar\omega+E_g)$ almost equals to 1, while $f_e(E+E_g)$ is very close to 0. Consequently, with photon energy $\hbar\omega$ and band gap E_g, the distribution of excited electrons with energy E is expressed as

$$\begin{aligned}N(E,\omega)=&N_A\cdot f_A(E_A)\cdot D_e(E)\cdot\delta(E-\hbar\omega+E_g-E_A)\\&+D_e(E)\cdot D_e(E-\hbar\omega)\cdot H(\hbar\omega-E_g-E),\end{aligned} \tag{6}$$

where $\delta(E)$ is the delta function and $H(E)$ is the Heaviside function. The first term describes the contribution from the acceptor level. $N_A\cdot f_A(E_A)$ is the acceptor level's contribution and $D_e(E)$ refers to the density at excited energy. In principle, electrons and holes are Fermions and they should not occupy the same states when coupling exist. However, since the density of the acceptors is low, the distance between two acceptors is far enough to decouple with each other. Therefore, the acceptors are assumed to stay at the same energy level [30]. The delta function is used to describe the energy distribution of excited electrons from the acceptor level. It can be inferred from the Eq. (6) that the initial energy of electrons from the acceptor level after excitation is $\hbar\omega-E_g+E_A$, while those from valence band lie in the range from 0 to $\hbar\omega-E_g$. Therefore, electrons from the acceptor level generally have higher energy and larger possibility to emit into vacuum.

After photon absorption, some of the excited electrons will move toward the surface for emission. We assume the distribution of the initial direction is isotropic. This assumption may have some deviations from the reality due to the penetration of applied electric field. If the photon energy is less than twice the band gap, the phonon scattering will be the dominant mechanism for the electron scattering. Here the analytical model only considers the energy loss during the scattering. The corresponding change of the trajectory motion is included in a Monte Carlo simulation, which will be discussed later. A semiclassical picture is used to determine the energy loss,

$$\triangle E=\frac{s}{x\sqrt{2E/m^*}}\cdot\lambda(E)\cdot E_{\mathrm{ph}}, \tag{7}$$

where x denotes $\cos\theta$ and θ is the direction of motion relative to the normal direction of the surface. s is the depth from the cathode surface where the electron absorbs a photon and gets excited. m^* is the electrons' effective mass and can be roughly estimated through [17]

$$m^*=\frac{E_g}{R_\infty}m_0 \tag{8}$$

where R_∞ is the Rydberg energy 13.606 eV.

$\lambda(E)$ in Eq. (7) refers to the scattering rate and E_{ph} is the phonon energy. For simplicity, we only consider the polar optical phonon scattering and intervalley scattering, since they have the most significant effect on the energy loss of electrons and the mean free path is short enough to exert influence on the states of excited electrons in the thin film. Acoustic phonon scattering is neglected due to its small phonon energy (~1 meV) and long mean free path, and hence less effect on electrons. When electrons lie in one band, polar optical phonon scattering is the dominate process. According to the previous references [28,32], the scattering rate from the polar optical phonon $\lambda_o(E)$ can be calculated through

$$\lambda_{o\pm}(E)=\frac{e^2m^{*\frac{1}{2}}E_{ph}(N_q+\frac{1}{2}\mp\frac{1}{2})}{4\sqrt{2}\pi\hbar^2\varepsilon_0\varepsilon_pE^{\frac{1}{2}}}\ln\left|\frac{(E\pm E_{ph})^{\frac{1}{2}}+E^{\frac{1}{2}}}{(E\pm E_{ph})^{\frac{1}{2}}-E^{\frac{1}{2}}}\right| \tag{9}$$

where $+/-$ means phonon absorption and emission respectively. ε_p is defined as the reciprocal of $(1/\varepsilon_\infty-1/\varepsilon_s)$ where ε_s and ε_∞ are material's static and high frequency dielectric constant, respectively. N_q is the occupation number of the phonon, following the Bose-Einstein statistics [30],

$$N_q=\frac{1}{\exp\left(E_{ph}/k_BT\right)-1}. \tag{10}$$

When electrons' energy is high enough to scatter into other valleys, intervalley scattering will be dominant. The corresponding scattering rate $\lambda_i(E)$ is much higher, leading to larger energy loss, and can be calculated as follows [28,32]

$$\lambda_{i\pm}(E)=\frac{D_i^2m^{*\frac{3}{2}}(N_q+\frac{1}{2}\mp\frac{1}{2})}{\sqrt{2}\pi\hbar^2\rho E_{ph}}(E\pm E_{ph})^{\frac{1}{2}} \tag{11}$$

where D_i is the deformation potential, which is often taken as 1×10^9 eV/cm, and ρ is the density of material.

As mentioned above, we are more interested in the energy loss during the scattering process. In a phonon scattering event, an electron can emit or absorb a phonon, resulting in the increase or decrease of energy by E_{ph}.

For most of the electrons' energy range, the possibility of emission is higher than that of the absorption. Therefore the scattering rate in Eq. (7) is $\lambda(E) = \lambda_{o-} - \lambda_{o+}$ for those electrons with energy lower than the minimum of the second lowest band and $\lambda(E) = \lambda_{o-} - \lambda_{o+} + \lambda_{i-} - \lambda_{i+}$ for those with higher energy.

When the electrons approach the surface, they will traverse the band bending region and obtain extra E_b in the longitudinal direction, as mentioned above. Finally, photoelectrons have to overcome the barrier to emit into the vacuum. The function $D(E)$ in Jensen's papers [17,33] is adopted here as the transmission probability, which is

$$D(E,\xi,E_a) = \frac{2}{1+\frac{(H(E)+E)}{2\sqrt{EH(E)}}[e^{\theta(E)} - \frac{1}{4}(1-e^{-\theta(E)})]}, \quad (12)$$

$$\theta(E) = \begin{cases} 0, & E > E_a \\ \frac{2}{\hbar e\xi}\sqrt{2m^*(E_a-E)^3}, & E \le E_a \end{cases} \quad (13)$$

$$H(E) = \sqrt{(E-E_a)^2 + (f_0^2\hbar^2(e\xi)^2/2m^*)^{\frac{2}{3}}}, \quad (14)$$

where ξ is the electric field and f_0 is a dimensionless number and the value is 0.51697. This expression connects the electron affinity E_a and electric field ξ to tunneling possibility. A higher electric field and a lower electron affinity will lead to a higher tunneling possibility.

The following is the derivation of the expression of QE and intrinsic emittance. Taking into account the transmission rate of photon, absorption rate by electrons and the possibility of emission, the expression of QE is given as

$$\frac{\mathrm{QE}}{1-R(\omega)} = \frac{\int_0^1\int_0^l\int_0^\infty N(E)F(s)T(E,s,x,\xi,E_a)\mathrm{d}E\mathrm{d}s\mathrm{d}x}{\int_0^\infty N(E)\mathrm{d}E\int_{-1}^1\mathrm{d}x}, \quad (15)$$

$$T(E,s,x,\xi,E_a) = D((E-\triangle E)x^2 + E_\mathrm{b},\xi,E_a), \quad (16)$$

$$F(s) = \alpha(\omega)e^{-\alpha(\omega)s}, \quad (17)$$

where $T(E,s,x,\xi,E_a)$ is the transmission possibility of electrons excited from the depth s with energy E and direction x [see Eq. (7)] to tunnel through the electron affinity E_a. $\triangle E$ is the energy loss defined in Eq. (7). l is the thickness of the cathode. $\alpha(\omega)$ is the photon absorption coefficient and $R(\omega)$ is the reflectivity, which vary with the laser angular frequency ω. $F(s)$ is the distribution of the position of excited electrons.

The intrinsic emittance is the normalized rms emittance at the cathode and it is related to the mean transverse energy (MTE) of emitted electrons through [26]

$$\epsilon_{xn} = \frac{1}{m_0c}\sqrt{\langle x^2\rangle\langle p_x^2\rangle} = \sigma_x\sqrt{\frac{\mathrm{MTE}}{m_0c^2}}. \quad (18)$$

Here σ_x is the rms laser size and $\langle p_x^2\rangle$ is the electrons' transverse momentum variance. c is the speed of light. It is assumed that the transverse position has no correlation with the transverse momentum [26], commonly used in the calculation of intrinsic emittance. The horizontal intrinsic emittance ϵ_{xn} should be theoretically the same with the vertical one ϵ_{yn}, since no $x-y$ asymmetry terms are present in our model. The conservation of transverse energy at the interface is assumed. Thus the MTE can be expressed as

$$\mathrm{MTE} = \frac{\int_0^1\int_0^l\int_0^\infty N(E)F(s)T(E,s,x,\xi,E_a)(1-x^2)EdEdsdx}{\int_0^1\int_0^l\int_0^\infty N(E)F(s)T(E,s,x,\xi,E_a)dEdsdx}. \quad (19)$$

The analytical model, including Eqs. (15) and (19), does not consider the change of electron's trajectory after scattering. A Monte Carlo simulation based on the analytical model is developed to examine this simplification. In the simulation, an electron is randomly generated at a position with given initial energy, following Eq. (17) and Eq. (6), respectively. The initial direction follows the isotropic assumption. The scattering rate is determined by Eqs. (9) and (11). In the simulation, the absorption and emission of phonon can be distinguished and thus a better evaluation of the energy change is available. When the electron's energy is lower than the minimum of the second lowest band, the scattering rate is given by $\lambda = \lambda_{o-} + \lambda_{o+}$. λ_{o-}/λ is the possibility to emit a phonon, leading to an energy loss of E_{ph}, while λ_{o+}/λ is the possibility to absorb a phonon, accompanied by an energy gain of E_{ph}. For electrons with energy above the minimum of the second lowest band, the scattering rate is $\lambda = \lambda_{o-} + \lambda_{o+} + \lambda_{i-} + \lambda_{i+}$, where $(\lambda_{o-} + \lambda_{i-})/\lambda$ is the possibility for phonon emission and $(\lambda_{o+} + \lambda_{i+})/\lambda$ is for phonon absorption. The electron's free time t can be derived from the scattering rate λ and the distribution is $f(t) = \exp(-t/t_1)$ where $t_1 = 1/\lambda$. During the free time, the electron drifts freely with velocity $v = \sqrt{2E/m^*}$, where E is energy and m^* is effective mass. A scattering event leads to an energy gain or loss of E_{ph} and changes the direction as well. The change of the direction is not isotropic, but following a specific distribution. The polar angle θ between the original and new trajectory and the azimuthal angle ϕ will follow the distributions [28,32],

$$g_1(\theta) \propto \frac{\sin\theta}{E + (E \pm E_{ph}) - 2\sqrt{E(E\pm E_{ph})}\cos\theta}, \quad (20)$$

$$g_2(\phi) = \frac{1}{2\pi}. \quad (21)$$

When the electron arrives at the surface, it should overcome the barrier to become a photoelectron. The possibility is decided in Eq. (12). If the electron eventually overcomes the barrier, its information will be recorded for the later calculation of QE and MTE.

In the following, Cs_3Sb is presented as an example to validate the above photoemission model by comparing to experimental results [12]. In the experiment, the incident photon energy is 1.8 eV (690 nm) and the QE and MTE are measured at two temperatures, 300 K and 90 K [12]. The band gap E_g and electron affinity E_a of Cs_3Sb are 1.6 eV and 0.3 eV, respectively. The acceptors in Cs_3Sb are believed to be the results of the cesium vacancies [34] and the energy E_A is 0.5 eV above the top of the valance band [35–37]. The contribution from acceptor level is significant at room temperature when the photon energy is near threshold but negligible at cryogenic environment. It is because $f_A(E_A)$ at 90 K in Eq. (3) is 5 orders of magnitude smaller than the value at 300 K and consequently the contribution from the acceptor level at 90 K can be neglected. Therefore, this is a suitable case for the validation of the model. The excited electrons from the valance band have energy below $(\hbar\omega - E_g) = 0.2$ eV while those from the acceptor level have energy around $(\hbar\omega - E_g + E_A) = 0.7$ eV. Since E_g is 1.6 eV, m^* in Eq. (8) would be 0.1176 m_0. The estimation is valid near the conduction band minimum, but not for those electrons with high energy. It can be inferred from the band diagram of Cs_3Sb the electrons with energy more than 0.6 eV stay at another band [38]. Therefore in both analytical and simulation calculation, electrons with energy below 0.6 eV have effective mass m^* as 0.1176 m_0 and those with energy above 0.6 eV have effective mass m^* as m_0. The effective mass is used in the calculation of drift velocity and the scattering rate.

Since the band bending energy has not been evaluated experimentally in the literature, it is treated as a flexible parameter to fit the experiment data[12] and the result is around 0.175 eV. The acceptor density N_A can be deduced from band bending energy in Eq. (1). It is found to be 1.586×10^{20} cm^{-3}, lying in the reported range [16,36]. Based on Eq. (1)–(3), the Fermi energy is derived to be located at 0.363 eV and the occupation possibility at acceptor level $f_A(E_A)$ would be 2.5×10^{-3}.

The photoemission results of Cs_3Sb with 1.8 eV photon energy against electric field are shown in Fig. 2 and the value of the relevant parameters can be found in Table I. The experimental [12], analytical and simulation results roughly agree with each other. In Fig. 2, the calculated MTE slightly decreases with electric field at 300 K while it increases at 90 K. The main difference between 300 K and 90 K is the participation of acceptor level in photoemission. At 90 K, the acceptor level is almost empty, so the photoelectrons are dominated by the valance band electrons. The increase of electric field reduces the tunneling barrier and leads to a higher MTE. At 300 K, the photoelectrons are dominated by electrons from the acceptor level, resulting in a higher MTE than at 90 K. The increase of electric field allows more valance band electrons to

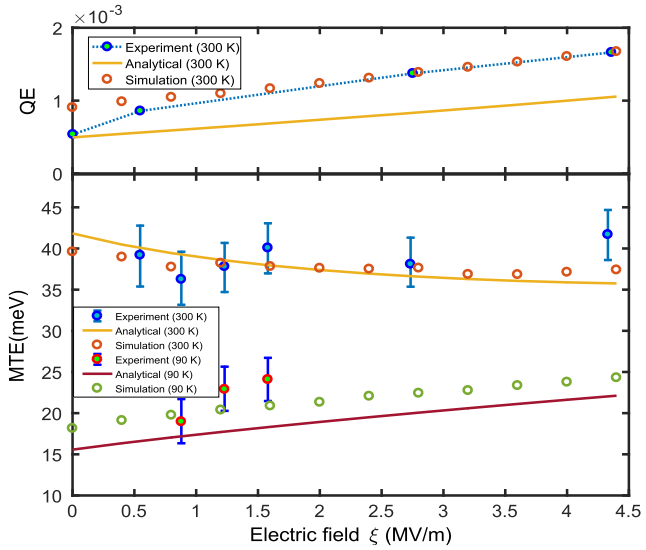

FIG. 2. Comparison between the analytical results, simulation results and the experiment data [12] in QE and MTE for Cs_3Sb threshold photoemission with 690 nm laser. The MTE plots include data points at two temperatures, 300 K and 90 K. The thickness of the photocathode is assumed to be 30 nm.

TABLE I. Parameter used for the case of Cs_3Sb.

Band gap E_g	1.6 eV [12]
Electron affinity E_a	0.3 eV [12]
Degraded electron affinity E_{a2}	0.4 eV [39]
Band bending energy E_b	0.175 eV (fit)[a]
Width of the band bending region d_b	1 nm [34]
Effective mass (E<0.6eV) m^*/m_0	0.1176 [17]
Effective mass (E>0.6eV) m^*/m_0	1
Photon absorption coefficient α	38277cm^{-1} (1.8 eV) [16]
	71332cm^{-1} (1.9 eV) [16]
	485197cm^{-1} (3.06 eV) [16]
Reflectivity R	23.11% (1.8 eV) [17]
	25.29% (1.9 eV) [17]
	32.04% (3.06 eV) [17]
Thickness l	30 nm [12]
Phonon energy E_{ph}	0.027 eV [18,40]
Energy of acceptor level E_A	0.5 eV [35–37]
Static dielectric constant ε_s	8.2 [17]
High frequency dielectric constant ε_∞	5.0 [17]
Oxygen partial pressure p_o	10^{-9} Torr
Density of oxygen atoms per layer N	5×10^{14} cm^{-2} [41,42]
Thickness of one layer d	0.3 nm [42,43]
Decay length L_d	6.1 nm (fit)[b]

[a]Obtained by fitting the experiment data in Fig. 2 with Eq. (15).
[b]Obtained by fitting the experiment data in Fig. 3 with Eqs. (15) and (28).

overcome the barrier. The contribution from acceptor level electrons decreases relatively and thus the MTE is reduced.

In the plot of QE, the analytical results are about two thirds of the simulation and there are mainly two reasons. The first reason is that the analytical calculation does not consider the trajectory change in the scattering events. For a material without boundary or with uniform electron excitation, the scattering will not cause differences between the forward current and the backward current. However, the cathode surface, as a boundary, should be considered in the photoemission study and a larger amount of electrons get excited near the surface [see Eq. (17)]. When the trajectory change is considered after a scattering, the excited electrons which move initially backward would still have opportunities to reach the surface due to back scattering, which is not possible in the analytical model. Simulations show the absence of trajectory change in scattering accounts for roughly 21% reduction of the QE in analytical models. The second reason is that the electrons continuously lose energy in the analytical model and the value is proportional to the transport distance, while in simulation the electron will not lose energy before a scattering event. As a result, after the last scattering, the electron loses a bit more energy in analytical model than in simulation. For threshold photoemission, the tunneling possibility is very sensitive to the electron energy. Therefore, the extra energy loss in analytical model leads to a lower tunneling possibility and thus a lower QE. Simulations show the energy loss after final scattering accounts for another 10% reduction of the QE results.

III. DYNAMIC MODEL

The static model discussed above does not include the surface degradation from the residual gases in vacuum. The continuous reduction of QE caused by the gas adsorption has been confirmed in experiments [23,44], while the impact on intrinsic emittance is not fully understood [25]. In the following, a dynamic model is established to describe the evolution of QE and intrinsic emittance during surface degradation process without ion back bombardment.

Many references have indicated that the residual gases have reaction with some elements of the cathodes and new composites form on the surface [45–47]. For most semiconductor photocathodes, the surface is cesium enriched to reduce the electron affinity. Cesium is chemically active and easily reacts with oxygen contained molecules. The newly formed layers, shown as the dash part in Fig. 1, will change the electron affinity and electron transmission probability. A higher electron affinity and thicker surface layer are the reasons for degradation.

To evaluate the evolution of electron affinity, we assume N_0 is the number of atoms of the original material on the surface of a fresh cathode. After reacting with the residual gas, the number of atoms of the original becomes N_1 and the number of atoms of the new composition is N_2. The original electron affinity is E_{a1} and the new composition's electron affinity is E_{a2}. The absorption rate is assumed to be proportional to N_1 with time constant τ. The time-dependent electron affinity of the contaminated surface can be derived as

$$\frac{dN_1}{dt} = -N_1/\tau \Rightarrow N_1 = N_0 \exp(-t/\tau), \tag{22}$$

$$N_2 = N_0 - N_1 = (1 - \exp(-t/\tau))N_0, \tag{23}$$

$$E_a(t) = \frac{N_1 E_{a1} + N_2 E_{a2}}{N_1 + N_2} = E_{a2} + (E_{a1} - E_{a2})e^{-t/\tau}. \tag{24}$$

The value of the electron affinity will gradually approach E_{a2}. Since E_{a2} is normally larger than E_{a1}, the photocathode will experience a QE degradation. The parameter τ is approximately the time for the formation of one layer and is evaluated as follows. Due to the low pressure, the gas molecules follow the ideal gas equation. They stay in a thermal equilibrium state and follow the Maxwell-Boltzmann distribution. As a result, the number of molecules n_1 that hit the surface in unit time and area is given as

$$\begin{aligned} n_1 &= n\left(\frac{m}{2\pi k_B T}\right)^{\frac{3}{2}} \iiint v_x \exp\left(-\frac{m}{2k_B T} v^2\right) d^3 v \\ &= n\sqrt{\frac{k_B T}{2\pi m}} = p\sqrt{\frac{1}{2\pi m k_B T}}, \end{aligned} \tag{25}$$

where p, T and k_B are pressure, temperature and Boltzmann constant, respectively. Mass m depends on the properties of the gases. If N is the density of molecules per layer, then τ can be estimated by

$$\tau = \frac{N}{\eta n_1}, \tag{26}$$

where η refers to the stoichiometry number of target element in the interested gas molecules. Here we have assumed the pressure p in n_1 is a time independent constant.

The absorption of oxygen also results in the thickness growth of the surface layer. The growth speed is simplified to be a constant of v_1. A rough estimation can be made by the thickness of one layer d divided by τ in Eq. (26).

The newly formed surface layer contains defects, impurities and recombination centers. Their presence leads to the loss of photoelectrons and reduce the possibility of emission. Therefore, a decay factor $T_1(t)$ is defined as,

$$T_1(t) = \begin{cases} \exp\left(-\frac{v_1 t}{L_d}\right), & t < \frac{d_{\max}}{v_1} \\ \exp\left(-\frac{d_{\max}}{L_d}\right) & t \geq \frac{d_{\max}}{v_1} \end{cases} \tag{27}$$

where L_d is the attenuation length, related to the condition of the surface layer. L_d cannot be derived analytically and it is left as a fitting number. $d_{\max}$ is the maximum thickness that the oxide layer can reach. There are some results that the degradation would stop at some point in a study from CERN [48]. It is hard to determine the value of $d_{\max}$, since it is related to the cathode surface and vacuum condition. Further studies are needed to derive an analytical expression for $d_{\max}$. $d_{\max}$ is not involved in the calculation of the following examples, since their QE degradations do not stop in the interested region.

Based on the above derivation, the time dependent emission possibility is

$$T(E, s, x, \xi, E_a(t), t) = D((E - \triangle E)x^2 + E_b, \xi, E_a(t))T_1(t). \quad (28)$$

The main differences between Eqs. (28) and (16) are the time dependant electron affinity $E_a(t)$ and the decay factor $T_1(t)$, corresponding to the two mechanisms. In dynamic model, Eq. (16) in the expressions for QE and MTE is replaced with Eq. (28).

The independent variable is time in the above discussion. A new parameter, oxygen dose D_o, is introduced below. It is the integration of oxygen partial pressure with time.

$$D_o(t) = \int_0^t p_o(\tau)d\tau. \quad (29)$$

The unit of D_o is Langmuir (L), which is 10^{-6} Torr s. When the oxygen partial pressure is time independent, the oxygen dose D_o is the product of the oxygen partial pressure and the time range. In the following discussions, the time t is replaced by the oxygen dose D_o.

Here a dynamic model is established to analyze the semiconductor photoemission degradation due to surface contamination. It has been confirmed that oxygen would result in a significant decrease of QE for GaAs in an experiment [44]. In addition, the first-principle calculation indicates that oxygen is the dominant poisonous gas to degrade alkali-based photocathodes [20]. Therefore, semiconductors degradation by oxygen can be representative for the influence of residual gases. The following discussion is based on the assumption that the effects of other oxygen containing molecules on the performance of the cathode are similar. Other elements are not considered in this model.

An oxygen controlled contamination experiment has been done on Cs_3Sb with incident photon energy 3.06 eV (405 nm) by a group from LANL [23]. The oxygen dominates the vacuum environment and the pressure is roughly 10^{-9} Torr. A fresh Cs_3Sb cathode is cesium enriched on the surface. The exposure in the oxygen enriched environment would result in the formation of cesium oxide on the surface. The electron affinity of cesium oxide Cs_2O is 0.4 eV. Since oxygen is the dominant gas here, the mass m in Eq. (25) is the mass of an oxygen molecule and the stoichiometry number η in Eq. (26) is 2. Under the condition of pressure 10^{-9} Torr and temperature 300 K, n_1 is calculated as 3.572×10^{11} cm^{-2} s^{-1} from Eq. (25). It is reported that the number of oxygen atoms per layer is about 5×10^{14} cm^{-2} [41,42]. Based on Eq. (26), the time constant τ is derived to be around 700 s. The thickness of one layer d is approximately 0.3 nm [42,43]. v_1 is estimated with the quotient of d and τ, which is 4.286×10^{-4} nm/s.

The QE degradation has been observed in the reference experiment and the fitting results from the presented model are shown in Fig. 3. The degradation can be divided into two stages. In the first stage, the increase of electron affinity is more important, leading to a fast QE decay. In the second stage, the electron affinity has almost reached a constant and the dominant term is the decay factor $T_1(t)$. A relatively slower decay is observed at this stage. The recesiation is able to reduce the electron affinity to the original level, but the deposition of extra cesium increases the thickness of the surface layer and the decay factor $T_1(t)$ would continue to exert its influence. This might be a reason why the QE is partly recovered after recesiation. Apart from the evolution of QE, the variation of the intrinsic emittance of photocathode can also be evaluated with an analytical model. The cathode intrinsic emittance decreases a little bit and stabilizes at about 0.762 mm mrad/mm rms, as shown in Fig. 3.

When the incident photon energy is lower than the emission threshold, things are more complicated and the acceptor level would have a great influence. Examples are taken on Cs_3Sb with the incident photon energy of 1.8 eV under the electric field of 4 MV/m and 50 MV/m,

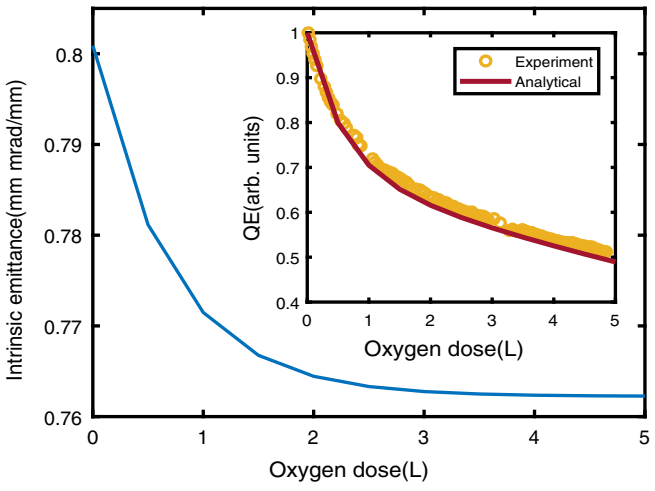

FIG. 3. The predicted time evolution of intrinsic emittance of Cs_3Sb from analytical model is presented as the blue line. The working condition, including oxygen pressure of 10^{-9} Torr and photon energy of 3.06 eV, is the same as in Ref. [23]. The inset shows the model fitting to Pavlenko's paper [23], which gives a L_d of 6.1 nm, shown in Table I. 1 Langmuir equals to 10^{-6} Torr s.

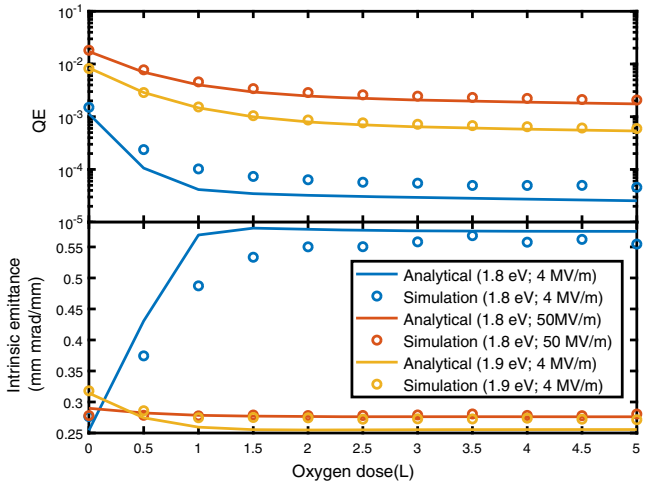

FIG. 4. The development of QE and intrinsic emittance of Cs_3Sb in the oxygen enriched environment with different incident photon energy and applied electric field. 1 Langmuir equals to 10^{-6} Torr s.

typical values for the DC gun and rf gun, as presented in Fig. 4. In simulation, every photoelectron's initial state is recorded and the ratio from the acceptor level is obtained, shown in Fig. 5. In Fig. 4, the analytical and the simulation results agree with each other. The QE degrades in both cases while the intrinsic emittance differs a lot. During the surface contamination, the intrinsic emittance at 4 MV/m considerably increases while it slightly decreases at 50 MV/m. The opposite performance can be explained by the differences of relative contribution from the acceptor level under two electric fields. In the model, the barrier of the cathode increases due to the surface oxidation and finally stays at a higher value. The transmission possibility of electrons from valance band will considerably decrease,

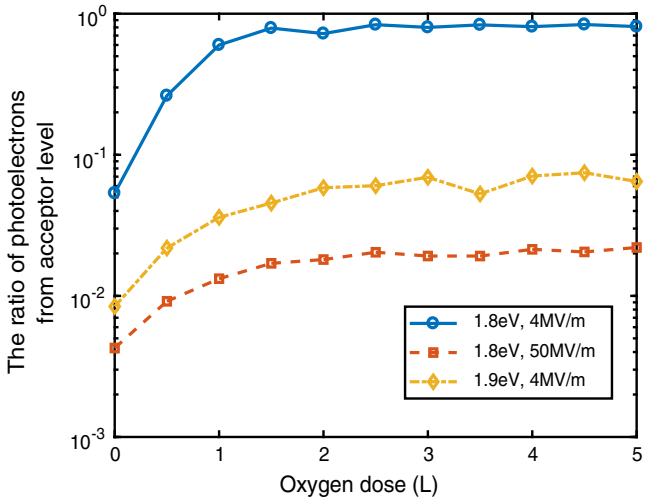

FIG. 5. The ratio of photoelectrons from acceptor level change under different conditions as shown in Fig. 4. All the results are obtained from the simulation.

while those from the acceptor level are hardly affected. At 4 MV/m, the increase of the barrier is the dominant factor and thus the acceptor level would gradually become the main source of photoelectrons. As shown in Fig. 5, the ratio of the acceptor level accounts for 80%. Since electrons from the acceptor level have higher energy, the intrinsic emittance is expected to increase. However, at 50 MV/m, the high electric field is able to compensate the opposite effect from the growing barrier. Therefore, the valence band electrons still dominate in the photoemission, which is important for a lower intrinsic emittance at threshold photoemission. There is another method to reduce the intrinsic emittance after oxidation at 4 MV/m, which is to raise the photon energy. As shown in Fig. 4, both QE and the intrinsic emittance with photon 1.9 eV get an improvement compared with those with photon 1.8 eV. It is a very interesting result for the intrinsic emittance, since the conventional formula (MTE $= (\hbar\omega - E_g - E_a)/3$) expects a higher intrinsic emittance with 1.9 eV photon [49,50]. The examples suggest that the acceptor level plays an important role in threshold photoemission at room temperature and the ratio between the contribution from the valance band and the acceptor level is sensitive to the working condition.

The model predicts that Cs_3Sb working at threshold photoemission under high electric field of 50 MV/m still has higher QE ($> 10^{-3}$) and lower intrinsic emittance ($\approx$0.28 mm mrad/mm rms) than copper, which is the most common metal cathode working at high electric field but driven by UV laser ($\sim$266 nm). As a comparison, the QE of copper is from 10^{-5} to 10^{-4}, depending on the surface cleanness and working condition, with the intrinsic emittance above 0.5 mm mrad/mm rms. However, the lifetime of Cs_3Sb is an important issue. When the oxide layers reach the maximum thickness d_{max}, the chemical robustness of the cathode is expected to be similar to the metal and a comparable lifetime is possible. It should also be noted that the lifetime of cathodes in the rf gun is affected by other factors as well, like laser and rf field [50]. Their influence on Cs_3Sb is not clear and more efforts should be devoted into the lifetime study experimentally. The response time is another key parameter for photocathodes. For copper, it is around 10^{-15} s. For semiconductors, it is related to incident photon energy [11,25]. Experimental data [12] indicate the response time of Cs_3Sb with incident photon energy of 1.8 eV is less than 1 ps. Based on the above analysis, a prediction is made that Cs_3Sb should be able to replace metal cathodes in normal conducting rf guns with a higher QE, lower intrinsic emittance and possible comparable lifetime, which is still to be confirmed experimentally.

Another controlled contamination experiment on GaAsP in oxygen enriched environment [25] is analyzed with the dynamic model. In the experiment, the incident laser is 532 nm (2.33 eV) and the oxygen pressure p_o is a constant of 10^{-10} Torr. By fitting to their results, it is discovered that

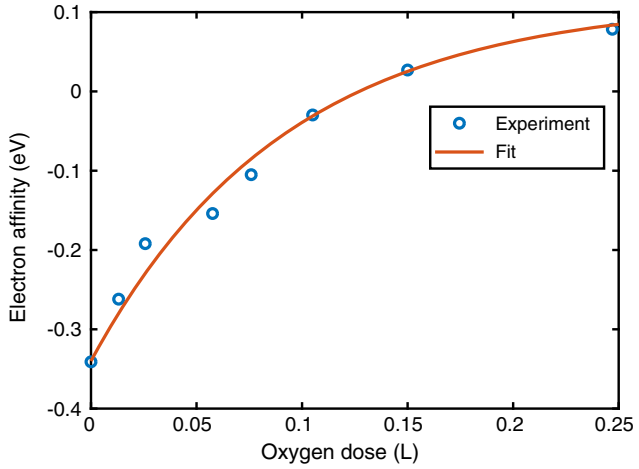

FIG. 6. The evolution of electron affinity of GaAsP during degradation process under oxygen enriched environment (10^{-10} Torr) with photon energy 2.33 eV (532 nm) in the experiment [25]. The fitting line from Eq. (30) is presented.

the growth of electron affinity during degradation can be well described by Eq. (24),

$$E_a(D_o) = E_{a2} + (E_{a1} - E_{a2}) \exp\left(-\frac{D_o}{\tau \times p_o}\right) = 0.117 + ((-0.34) - 0.117) \times \exp\left(-\frac{D_o}{0.0924}\right). \tag{30}$$

Here the independent variable is replaced by the oxygen dose D_o instead of the time t. The values of E_{a1}, E_{a2} and τ are obtained from the fitting, shown in Fig. 6. Good agreement has been achieved with the experimental data.

As for the decay factor $T_1(t)$, it can be expressed with oxygen dose as an independent variable, shown as

$$T_1(t) = \exp\left(-\frac{v_1 t}{L_d}\right) = \exp\left(-\frac{t \cdot p_o}{N\sqrt{2\pi m k_B T} L_d}\right) = \exp\left(-\frac{D_o}{0.0285}\right) = T_1(D_o). \tag{31}$$

With the above derivation and the listed parameter in Table II, the Monte Carlo simulation based on the proposed model is applied to reproduce the data in the GaAsP experiment at room temperature. The simulation results of both QE and MTE have good agreement with experimental data. It is a strong support to the proposed dynamic model. As displayed in Fig. 7(b), the MTE decreases by more than 40% after exposure to oxygen. The MTE reaches a plateau when the electron affinity is close to zero, and the reason is as following. Many electrons accumulate at the bottom of

TABLE II. Parameter used for the case of GaAsP.

Band gap E_g	1.723 eV [51]
Electron affinity E_a	−0.34 eV [25]
Degraded electron affinity E_{a2}	0.117 eV [25]
Band bending energy E_b	0.54 eV [27]
Width of the band bending region d_b	9 nm [27]
Effective mass m^*/m_0	1
Photon absorption coefficient α	60000 cm^{-1} (2.33 eV) [52]
Reflectivity R	65% (2.33 eV) [53]
Phonon energy E_{ph}	0.029 eV [27]
Static dielectric constant ε_s	13.18 [27]
High frequency dielectric constant ε_∞	10.89 [27]
Oxygen partial pressure p_o	10^{-10} Torr [25]
Density of oxygen atoms per layer N	5×10^{14} cm^{-2} [41,42]
Thickness of one layer d	0.3 nm [42,43]
Decay length L_d	0.04 nm (ad hoc)[a]

[a]Obtained by fitting the experiment data in Fig. 7.

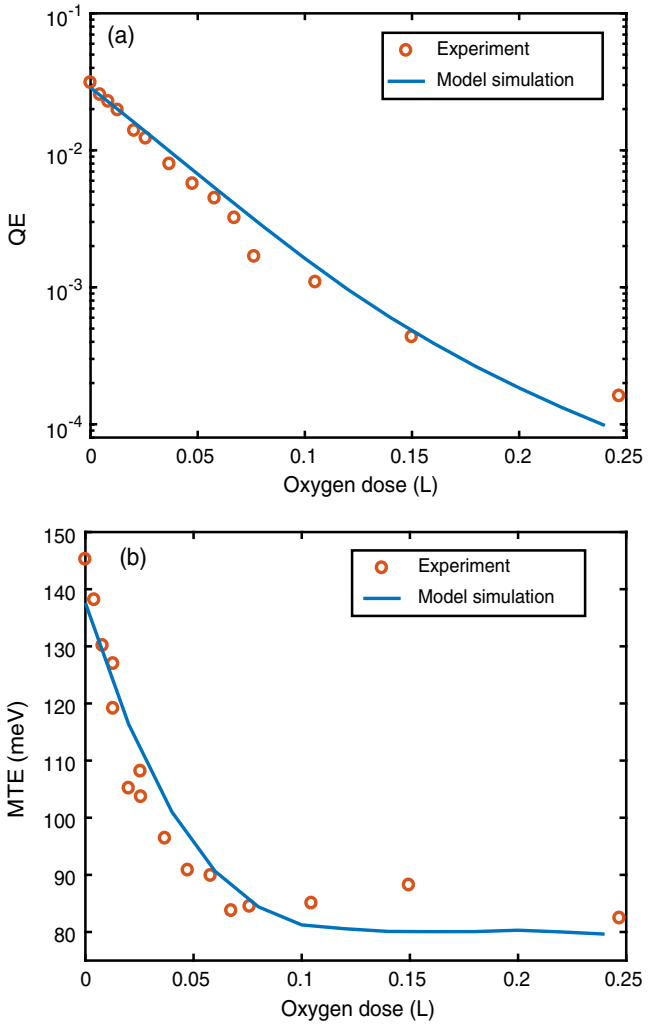

FIG. 7. The evolution of QE and MTE of GaAsP during degradation process under oxygen enriched environment (10^{-10} Torr) with photon energy 2.33 eV (532 nm) in the experiment [25]. (a) is about QE and (b) is about MTE. The monte carlo simulation results on QE and MTE are also presented respectively.

the conduction band during transport to the cathode surface due to multiple scatterings with phonons. They have very low energy and thus very low MTE. These low energy electrons transmission probabilities are sensitive to the increase of the vacuum barrier. Therefore, their weight in photoelectrons drops significantly after the electron affinity reaches zero, leading to a larger MTE. Meanwhile, the excess energy of the photoelectrons decreases due to the increase of the barrier, leading to a lower MTE. The interplay of the two opposite effects results in a MTE plateau near the zero electron affinity region.

IV. DISCUSSION AND SUMMARY

A Monte Carlo simulation on Cs_3Sb was presented in the Ref. [19]. The simulation is specifically for Cs_3Sb and the detailed band structures of Cs_3Sb from density functional theory calculations are applied. The simulation in this paper does not limit the discussions to Cs_3Sb and thus the common parabola shape energy band is used. Some parameters are adopted with different values, like the energy of acceptor level above the valance band and the electron affinity. The intervalley scattering is considered for the high energy electrons in our simulation, which is neglected in the reference paper. Despite some differences, the treatment of acceptor level as a mono energy level in the band gap in our simulation is similar to the isolated acceptor level in Sakata scenarios in the reference paper.

Some photoemission physics are not discussed in this paper. For example, we ignore the surface roughness which tends to increase the emittance [54–56], especially at high cathode gradient. The laser heating effect is not included. Our model also neglects the possible variation of the band gap with temperature and the details of band structure for the specific materials. In the dynamic model, we do not consider the ion back bombardment, which is another important reason for the degradation of cathode performance. Further extensions should include these impacts. The decay length L_d in Eq. (29) should be well defined in future work. Despite the above simplifications, our model achieved satisfying agreements with experiment data on different materials from different groups.

In summary, an improved model of semiconductor photoemission with the consideration of acceptor level has been proposed to evaluate the cathode performance near threshold emission. The experimental data of the QE and MTE of Cs_3Sb under different electric fields can be reproduced by the model. A dynamic model is also proposed to understand the physical process in the QE degradation of cathodes due to residual gases absorption. The model has been applied to analyze two examples, including the QE degradation of Cs_3Sb and the evolution of the electron affinity, QE and MTE of GaAsP under oxygen enriched environment, and good agreement has been achieved with the experimental data. The simulation results suggest that the performance of near threshold emission of oxidized Cs_3Sb cathode may be better than UV photoemission of metal cathodes in terms of both QE and thermal emittance. With the oxidization layer, the tolerance of semiconductor cathode to gun vacuum condition may be comparable to metal cathode, which needs further test in experiment. The dynamic photoemission model in this paper not only helps experiment efforts toward realizing next generation low emittance semiconductor cathodes, but also gives a new direction for semiconductor cathode applications in photoinjectors.

This work is supported by Science Challenge Project No. TZ2018005.

[1] C. Bostedt, S. Boutet, D. M. Fritz, Z. Huang, H. J. Lee, H. T. Lemke, A. Robert, W. F. Schlotter, J. J. Turner, and G. J. Williams, Linac coherent light source: The first five years, Rev. Mod. Phys. **88**, 015007 (2016).

[2] S. Boutet, L. Lomb, G. J. Williams, T. R. Barends, A. Aquila, R. B. Doak, U. Weierstall, D. P. DePonte, J. Steinbrener, R. L. Shoeman *et al.*, High-resolution protein structure determination by serial femtosecond crystallography, Science **337**, 362 (2012).

[3] H. N. Chapman, X-ray imaging beyond the limits, Nat. Mater. **8**, 299 (2009).

[4] V. R. Morrison, R. P. Chatelain, K. L. Tiwari, A. Hendaoui, A. Bruhács, M. Chaker, and B. J. Siwick, A photoinduced metal-like phase of monoclinic VO_2 revealed by ultrafast electron diffraction, Science **346**, 445 (2014).

[5] R. P. Chatelain, V. R. Morrison, B. L. M. Klarenaar, and B. J. Siwick, Coherent and Incoherent Electron-Phonon Coupling in Graphite Observed with Radio-Frequency Compressed Ultrafast Electron Diffraction, Phys. Rev. Lett. **113**, 235502 (2014).

[6] S. Weathersby, G. Brown, M. Centurion, T. Chase, R. Coffee, J. Corbett, J. Eichner, J. Frisch, A. Fry, M. Gühr *et al.*, Mega-electron-volt ultrafast electron diffraction at SLAC National Accelerator Laboratory, Rev. Sci. Instrum. **86**, 073702 (2015).

[7] I. V. Bazarov, B. M. Dunham, and C. K. Sinclair, Maximum Achievable Beam Brightness from Photoinjectors, Phys. Rev. Lett. **102**, 104801 (2009).

[8] S. Karkare, J. Feng, X. Chen, W. Wan, F. J. Palomares, T.-C. Chiang, and H. A. Padmore, Reduction of Intrinsic Electron Emittance from Photocathodes Using Ordered Crystalline Surfaces, Phys. Rev. Lett. **118**, 164802 (2017).

[9] B. L. Rickman, J. A. Berger, A. W. Nicholls, and W. A. Schroeder, Intrinsic Electron Beam Emittance from Metal Photocathodes: The Effect of the Electron Effective Mass, Phys. Rev. Lett. **111**, 237401 (2013).

[10] M. C. Divall, E. Prat, S. Bettoni, C. Vicario, A. Trisorio, T. Schietinger, and C. P. Hauri, Intrinsic emittance reduction of copper cathodes by laser wavelength tuning in an rf photoinjector, Phys. Rev. ST Accel. Beams **18**, 033401 (2015).

[11] I. V. Bazarov, B. M. Dunham, Y. Li, X. Liu, D. G. Ouzounov, C. K. Sinclair, F. Hannon, and T. Miyajima, Thermal emittance and response time measurements of negative

electron affinity photocathodes, J. Appl. Phys. **103**, 054901 (2008).
[12] L. Cultrera, S. Karkare, H. Lee, X. Liu, I. Bazarov, and B. Dunham, Cold electron beams from cryocooled, alkali antimonide photocathodes, Phys. Rev. ST Accel. Beams **18**, 113401 (2015).
[13] L. Cultrera, C. Gulliford, A. Bartnik, H. Lee, and I. Bazarov, Ultra low emittance electron beams from multi-alkali antimonide photocathode operated with infrared light, Appl. Phys. Lett. **108**, 134105 (2016).
[14] J. Feng, J. Nasiatka, W. Wan, S. Karkare, J. Smedley, and H. A. Padmore, Thermal limit to the intrinsic emittance from metal photocathodes, Appl. Phys. Lett. **107**, 134101 (2015).
[15] J. Maxson, L. Cultrera, C. Gulliford, and I. Bazarov, Measurement of the tradeoff between intrinsic emittance and quantum efficiency from a NaKSb photocathode near threshold, Appl. Phys. Lett. **106**, 234102 (2015).
[16] W. E. Spicer, Photoemissive, photoconductive, and optical absorption studies of alkali-antimony compounds, Phys. Rev. **112**, 114 (1958).
[17] K. L. Jensen, B. L. Jensen, E. J. Montgomery, D. W. Feldman, P. G. OShea, and N. Moody, Theory of photoemission from cesium antimonide using an alpha-semiconductor model, J. Appl. Phys. **104**, 044907 (2008).
[18] H. Xie, I. Ben-Zvi, T. Rao, T. Xin, and E. Wang, Experimental measurements and theoretical model of the cryogenic performance of bialkali photocathode and characterization with Monte Carlo simulation, Phys. Rev. Accel. Beams **19**, 103401 (2016).
[19] P. Gupta, L. Cultrera, and I. Bazarov, Monte Carlo simulations of electron photoemission from cesium antimonide, J. Appl. Phys. **121**, 215702 (2017).
[20] G. Wang, R. Pandey, N. A. Moody, and E. R. Batista, Degradation of alkali-based photocathodes from exposure to residual gases: A first-principles study, J. Phys. Chem. C **121**, 8399 (2017).
[21] D. Filippetto, H. Qian, and F. Sannibale, Cesium telluride cathodes for the next generation of high-average current high-brightness photoinjectors, Appl. Phys. Lett. **107**, 042104 (2015).
[22] T. Wada, T. Nitta, T. Nomura, M. Miyao, and M. Hagino, Influence of Exposure to CO, CO2 and H2O on the Stability of GaAs Photocathodes', Japanese J. Appl. Phys. **29**, 2087 (1990).
[23] V. Pavlenko, F. Liu, M. A. Hoffbauer, N. A. Moody, and E. R. Batista, Kinetics of alkali-based photocathode degradation, AIP Adv. **6**, 115008 (2016).
[24] E. Chevallay, Experimental results at the C.E.R.N. photoemission laboratory with co-deposition photocathodes in the frame of the CLIC studies, CLIC, CERN Internal Note Report No. CTF3-Note-2012-104, 2012.
[25] L. Jones, H. Scheibler, D. Gorshkov, A. Terekhov, B. Militsyn, and T. Noakes, Evolution of the transverse and longitudinal energy distributions of electrons emitted from a GaAsP photocathode as a function of its degradation state, J. Appl. Phys. **121**, 225703 (2017).
[26] D. H. Dowell and J. F. Schmerge, Quantum efficiency and thermal emittance of metal photocathodes, Phys. Rev. Accel. Beams **12**, 074201 (2009).
[27] S. Karkare, D. Dimitrov, W. Schaff, L. Cultrera, A. Bartnik, X. Liu, E. Sawyer, T. Esposito, and I. Bazarov, Monte Carlo charge transport and photoemission from negative electron affinity GaAs photocathodes, J. Appl. Phys. **113**, 104904 (2013).
[28] L. Ye *et al.*, *Semiconductor Physics* (China Higher Education Press, CHEP, Beijing, 2009), Vol. 202.
[29] V. Heine, Theory of surface states, Phys. Rev. **138**, A1689 (1965).
[30] C. Kittel, *Introduction to Solid State Physics*, 8th ed. (John Wiley & Sons, New York, 2005).
[31] D. H. Dowell, F. K. King, R. E. Kirby, J. F. Schmerge, and J. M. Smedley, In situ cleaning of metal cathodes using a hydrogen ion beam, Phys. Rev. Accel. Beams **9**, 063502 (2006).
[32] W. Fawcett, A. Boardman, and S. Swain, Monte Carlo determination of electron transport properties in gallium arsenide, J. Phys. Chem. Solids **31**, 1963 (1970).
[33] K. L. Jensen, Electron emission theory and its application: Fowler–Nordheim equation and beyond, J. Vac. Sci. Technol. B **21**, 1528 (2003).
[34] W. E. Spicer, Photoemission and related properties of the alkali-antimonides, J. Appl. Phys. **31**, 2077 (1960).
[35] Z. Lin and X. Wang, *Cathode Electronics(in Chinese)* (National Defence Industry Press, Beijing, 2013).
[36] T. Sakata, Studies on. the Cs_3Sb Photo-Cathode, J. Phys. Soc. Jpn. **8**, 723 (1953).
[37] C. Lee, Photoelectron energy distribution of Cs_3Sb, J. Appl. Phys. **54**, 4578 (1983).
[38] L. Kalarasse, B. Bennecer, F. Kalarasse, and S. Djeroud, Pressure effect on the electronic and optical properties of the alkali antimonide semiconductors Cs_3Sb, KCs_2Sb, CsK_2Sb and K_3Sb: Ab initio study, J. Phys. Chem. Solids **71**, 1732 (2010).
[39] C. W. Bates, Jr., Low-temperature thermionic emitters using metal-semiconductor composites, Mater. Lett. **23**, 1 (1995).
[40] V. Beguchev, I. Shefova, and A. Musatov, Optical and photoemissive properties of multi-alkali photocathodes, J. Phys. D **26**, 1499 (1993).
[41] G. Vergara, L. Gomez, J. Capmany, and M. Montojo, Adsorption kinetics of cesium and oxygen on GaAs(100): A model for the activation layer of GaAs photocathodes, Surf. Sci. **278**, 131 (1992).
[42] C. Su, W. E. Spicer, and I. Lindau, Photoelectron spectroscopic determination of the structure of (Cs,O) activated GaAs (110) surfaces, J. Appl. Phys. **54**, 1413 (1983).
[43] D. Fisher, R. Enstrom, J. Escher, and B. Williams, Photoelectron surface escape probability of (Ga,In)As : Cs-O in the 0.9 to [inverted lazy s] 1.6 μm range, J. Appl. Phys. **43**, 3815 (1972).
[44] N. Chanlek, J. Herbert, R. Jones, L. Jones, K. Middleman, and B. Militsyn, The degradation of quantum efficiency in negative electron affinity GaAs photocathodes under gas exposure, J. Phys. D **47**, 055110 (2014).
[45] C. Bates, Jr., T. M. Van Atekum, G. Wertheim, D. Buchanan, and K. Clements, X-ray photoemission studies of superficially oxidized cesium antimonide photoemitters, Appl. Phys. Lett. **38**, 387 (1981).

[46] I. Martini, E. Chevallay, V. Fedosseev, C. Hessler, H. Neupert, V. Nistor, and M. Taborelli, X-ray photoemission spectroscopy studies of cesium antimonide photocathodes for photoinjector applications, Phys. Procedia **77**, 34 (2015).

[47] A. Di Bona, F. Sabary, S. Valeri, P. Michelato, D. Sertore, and G. Suberlucq, Auger and x-ray photoemission spectroscopy study on Cs_2Te photocathodes, J. Appl. Phys. **80**, 3024 (1996).

[48] E. Chevallay, G. Suberlucq, and H. Trautner, Production of a high average current electron beam with Cs-Te photocathodes, CLIC, CERN Report No. CTF3 Note020, 2001.

[49] D. Dowell, I. Bazarov, B. Dunham, K. Harkay, C. Hernandez-Garcia, R. Legg, H. Padmore, T. Rao, J. Smedley, and W. Wan, Cathode R&D for future light sources, Nucl. Instrum. Methods Phys. Res., Sect. A **622**, 685 (2010).

[50] F. Le Pimpec, C. Milne, C. Hauri, and F. Ardana-Lamas, Quantum efficiency of technical metal photocathodes under laser irradiation of various wavelengths, Appl. Phys. A **112**, 647 (2013).

[51] A. Alahmary, N. Bouarissa, and A. Kamli, Band structure and lattice vibration properties of III-P ternary alloys, Physica B (Amsterdam) **403**, 1990 (2008).

[52] M. D. Sturge, Optical absorption of gallium arsenide between 0.6 and 2.75 eV, Phys. Rev. **127**, 768 (1962).

[53] G. D. Clark, Jr. and N. Holonyak, Jr., Optical properties of gallium arsenide-phosphide, Phys. Rev. **156**, 913 (1967).

[54] X. Z. He, C. X. Tang, W. H. Huang, and Y. Z. Lin, Researches on thermal emittance of metal cathode in photoinjectors, Chin. Phys. C **28**, 1007 (2004).

[55] H. J. Qian, C. Li, Y. C. Du, L. X. Yan, J. F. Hua, W. H. Huang, and C. X. Tang, Experimental investigation of thermal emittance components of copper photocathode, Phys. Rev. Accel. Beams **15**, 040102 (2012).

[56] Z. Zhang and C. Tang, Analytical study on emittance growth caused by roughness of a metallic photocathode, Phys. Rev. Accel. Beams **18**, 053401 (2015).